coatings

MDPI

Article

First Approach to ZrB_2 Thin Films Alloyed with Silver Prepared by Magnetron Co-Sputtering

Tomáš Fiantok [1,*], Martin Truchlý [1], Viktor Šroba [2], Tomáš Roch [2], Vitalii Izai [1], Marek Vidiš [1], Marián Haršáni [3], Leonid Satrapinskyy [2] and Marián Mikula [2,4]

[1] Detached Workplace of Faculty of Mathematics, Physics and Informatics, Comenius University in Bratislava, Sadová 1148, 038 53 Turany, Slovakia
[2] Department of Experimental Physics, Faculty of Mathematics, Physics and Informatics, Comenius University in Bratislava, Mlynská Dolina F2, 842 48 Bratislava, Slovakia
[3] Staton, s.r.o., Sadová 1148/9, 038 53 Turany, Slovakia
[4] Institute of Materials and Machine Mechanics, Slovak Academy of Sciences, Dúbravská Cesta 9, 845 11 Bratislava, Slovakia
* Correspondence: tomas.fiantok@fmph.uniba.sk; Tel.: +421-918-588-520

Abstract: Hexagonal ZrB_2 belongs to the group of ultra-high temperature ceramics representing an important class of materials with the potential to meet the high demands of today's industry. However, this potential is limited by inherent brittleness and poor tribological properties. Here, the combination of density functional theory and experiment is used to investigate the effect of silver alloying on the mechanical and tribological properties of hexagonal ZrB_2 thin films. Calculations indicate strong insolubility of Ag atoms in the ZrB_2 metal sublattice and a significant effect on the mechanical properties, pointing out an improvement in ductility and tribological properties but at the cost of reduced hardness. The experiments confirmed the theoretical predictions of the strong insolubility of silver, where the magnetron-sputtered $Zr_{1-x}Ag_xB_{2+\Delta}$ films form a segregated nanostructure consisting of separated hexagonal ZrB_2 and cubic Ag phases. With increased Ag content, values of Young's modulus decrease from $E^{ZrB2.31}$ = 375 GPa to $E^{Zr0.26Ag0.74B0.89}$ = 154 GPa, followed by a decrease in hardness from $H^{ZrB2.31}$ = 30 GPa to a value of $H^{Zr0.26Ag0.74B0.89}$ = 4 GPa. The suppression of crack formation is also shown with the material flow around cube corner indents, indicating enhanced ductility. The improvement of tribological properties was also confirmed when the coefficient of friction (COF) was reduced from $COF^{ZrB2.31}$ ~0.9 to a value of $COF^{Zr0.26Ag0.74B0.89}$ ~0.25 for all counterpart materials—steel (100Cr6), Si_3N_4, and WC/Co.

Keywords: zirconium diboride; silver; DFT; tribological properties; enhanced ductility

Citation: Fiantok, T.; Truchlý, M.; Šroba, V.; Roch, T.; Izai, V.; Vidiš, M.; Haršáni, M.; Satrapinskyy, L.; Mikula, M. First Approach to ZrB_2 Thin Films Alloyed with Silver Prepared by Magnetron Co-Sputtering. *Coatings* **2023**, *13*, 663. https://doi.org/10.3390/coatings13030663

Academic Editor: Jeon Geon Han

Received: 20 February 2023
Revised: 17 March 2023
Accepted: 20 March 2023
Published: 22 March 2023

1. Introduction

Transition metal diborides (TMB_2), compounds of boron, and transition metal (TM) from IV.—VI. groups (Ti, V, Cr, Zr, Nb, Mo, Hf, Ta, and W) [1] have received much attention in terms of their excellent properties such as extremely high melting temperature, chemical and thermal stability, high hardness, and high thermal and electrical conductivity. These exceptional characteristics predispose these materials to be used in extremely demanding space applications [2–6].

TMB_2 thin films are most often synthesized by physical vapor deposition (PVD) techniques, most likely by magnetron sputtering in a non-reactive argon atmosphere. In this specific case, the deposition process is accompanied by two dominant effects: (i) Different angular distribution of light boron and heavy metal atoms [7]. (ii) The effect of resputtering of the growing film with reflected Ar neutrals. The two effects lead to significant changes in the stoichiometry, structure, and mechanical properties of the TMB_2 films [8].

Overstoichiometry in TMB_2 films is typical for light TM atoms (Ti, Zr). Such films consist of a nanocomposite structure composed of stoichiometric grains (nanofilaments) separated by an amorphous B-tissue phase [6,9]. On the other hand, the effect of resputtering, typical for heavy TM atoms (Hf, Ta, W, ...), leads to the formation of understoichiometric films with grains containing vacancies in boron sublattice or the structure is completely amorphous [8].

The fundamental weakness of TMB_2 films is their brittle nature (expressed by high values of Young's modulus) [8,9]. In recent years, several approaches have been investigated to improve the ductility/toughness of ceramic thin films, e.g., structural modification of nanocomposites, vacancy engineering [8,10,11], strengthening through multilayer structures [12–14] or multicomponent alloying [9,15,16].

Recent research activities proved the positive influence of alloying on mechanical properties. Alloying of ZrB_2 films with Ta is manifested by a hardness increase from 35 to 42 GPa and an increase in indentation toughness from 4 to 5.2 MPa.$m^{-1/2}$ [16]. ZrB_2 thin films alloyed with only 8 at.% of Al show a decrease in Young's modulus of more than 20% compared with that of pure $ZrB_{2.2}$. This indirectly indicates the improvement toward ductile behavior [9]. Similarly, Nedfors et al. [15] observed a decrease in Young's modulus of approx. 18% from pure TiB_2 after alloying of 8 at.% of Al.

Another weakness of TMB_2 films is their relatively high coefficient of friction in humid air [17–19], which excludes these materials from a large number of tribological applications. Concerning the tribological properties, several authors report the coefficient of friction (COF) of bulk ZrB_2 to be in the interval from 0.2 to 0.9 depending on the choice of measurement, load, surface morphology, chemical composition, environment, and material of the counterpart. Umeda et al. [17] pointed out the strong dependence of COF on environmental conditions. A typical value of the COF of sintered ZrB_2 versus its ZrB_2 counterpart is approximately 0.95 at humidity below 20%, but 0.4 at a humidity above 90%. Sonber et al. [20] investigated the behavior of sintered ZrB_2 against a WC/Co ball at various loads and frequencies, at ambient conditions, and at 50% relative humidity. The COF was evaluated between 0.8 and 0.4 at different loads and sliding frequencies, where increasing the load and decreasing the frequency decreased the COF from 0.84 to 0.43. There are several studies [21,22] investigating the tribological properties of ZrB_2-(B_4C, ZrC, SiC) composites with a positive effect on COF reduction. Still, to our best knowledge, the impact of alloying ZrB_2 with silver on the mechanical and tribological properties has not yet been investigated.

However, several studies [23,24] can be found on the investigation of the influence of Ag alloying on TM-Nitrides (TM—Zr, Ti, Mo, ...), indicating improvement of tribological properties. Moreover, silver itself shows positive lubricating properties [25]. Thus, $TMAgB_2$ represent a potential coating candidate with extraordinary mechanical and tribological properties on various type of substrates.

In this work, ZrB_2 was chosen as a prospective hard coating to demonstrate the influence of silver alloying on the mechanical and tribological properties. Plain ZrB_2 is a highly stable ceramic material with a melting temperature of 3246 °C and excellent mechanical properties due to strong covalent and ionic-covalent bonds between atoms [9,26]. Here, we combine theoretical predictions of phase stability and mechanical properties of α-$Zr_{1-x}Ag_xB_2$ using density functional theory (DFT) with experimental investigation of $Zr_{1-x}Ag_xB_2$ films prepared by magnetron sputtering. DFT calculations indicate a strong tendency towards phase separation of the α-$Zr_{1-x}Ag_xB_2$ solid solution. From the point of view of mechanical properties, increasing the concentration of silver in α-$Zr_{1-x}Ag_xB_2$ leads to more ductile behavior and improved lubrication properties, but it is accompanied by a decrease in hardness. The experimental results are in good agreement with the ab initio predictions and confirm the insolubility of silver in the ZrB_2 phase. The effect of Ag alloying was manifested in the reduction of hardness, as the hardness value decreased from 30 GPa for Ag-free ZrB_2 films to 4 GPa for the film with 39 at.% Ag. The

coefficient of friction was reduced by adding silver from 0.95 for ZrB_2 to 0.25 for the sample with 39 at.% Ag.

2. Materials and Methods

2.1. Calculation Methods

DFT calculations were carried out using QUANTUM ESPRESSO v. 6.4.1, employing projector-augmented wave pseudopotentials [27] and the Perdew–Burke–Ernzerhof parametrization [28,29] of the electronic exchange-correlation functionals. The α-$Zr_{1-x}Ag_xB_2$ solid solution, with x $\in$ (0,1), was simulated using a 2 × 2 × 2 supercell (24 atoms). Overall, nine different compositions moving from stoichiometric ZrB_2 to AgB_2 (with a step in x of 0.125) were investigated, where Ag atoms randomly substituted Zr atoms. The influence of different choices of Ag substitution on results was also verified by comparison of total energies of various random configurations (for the same Ag content), resulting in only small differences up to 0.01 eV/at. Total energy and lattice parameters of all structures were determined by relaxing cell shapes, volumes, and atomic coordinates using a 9 × 9 × 9 k-point grid for Brillouin-zone sampling and a plane wave energy cutoff of 90 Ry, while imposing the convergence criteria of 10^{-7} Ry for energies and 10^{-5} Ry/bohr for forces. The chosen energy cutoffs and numbers of k-points ensured energy convergence within a few meV/atom. The stability of the α-$Zr_{1-x}Ag_xB_2$ in the form of a solid solution was investigated in terms of formation energy E_f [9] and mixing enthalpy ΔH_{mix} [9].

Ab-initio mechanical properties were computed using the THERMO-PW driver as implemented in QUANTUM-ESPRESSO routines. α-$Zr_{1-x}Ag_xB_2$ solid solutions were investigated from the view of mechanical stability, where the elastic constants C_{ij} must meet the necessary conditions of mechanical stability. From the elastic constants of stable systems, we calculated the bulk modulus (B) and shear modulus (G) by the Voight–Reuss–Hill approximation [30]. Furthermore, to discuss mechanical properties, Young's modulus (E) and Poison's ratio (ν) were also estimated [30]. Vickers hardness H_v was approximated from an empirical formula proposed by Chen et al. [31]. Moreover, the ductile/brittle behavior was investigated from the view of Cauchy's pressures and Pugh's indicator (G/B). Parameter $\mu_m = B/C_{44}$, known as the machinability index, assesses the suitability of materials for industrial applications, where large values of μ_m (values of order 10 and more) indicate excellent lubricant properties of materials [32].

2.2. Experimental Materials and Methods

The $Zr_{1-x}Ag_xB_{2+\Delta}$ films were prepared by non-reactive direct current (DC) co-sputtering from ceramic ZrB_2 (100 mm in diameter, 99.5 at.%, RHP Technology, Seibersdorf, Austria) and metal Ag (100 mm in diameter, 99.99 at.%, Kremnica Mint, Kremnica, Slovakia) targets in self-made deposition equipment. A chromium target (100 mm in diameter, 99.5 at.%, Testbourne, Basingstoke, UK) was used for the deposition of the 100 nm thick Cr buffer layer. After 5 min deposition of the Cr buffer layer, there was an additional 1 min where all three cathodes (ZrB_2, Ag, Cr) deposited an interdiffusion layer to ensure a smoother transition from the buffer into the main layer. The mirror-polished c-cut sapphire (0001), silicon (001), and steel (K100, S600) plates were used as substrates. Silicon substrates were only used for chemical analysis, morphology, and x-ray diffraction measurements. Substrates were placed on the heated (400 °C) and non-biased (floating potential) holder located in the intersection of the three magnetrons—two magnetrons tilted at 45° with respect to substrates normal, one magnetron (Cr target) situated directly opposite the rotatable substrate holder. The distance of the substrates from the side magnetrons was set to approximately 15 cm and approximately 19 cm from the Cr target. Before deposition, the chamber was evacuated to the base pressure of 5 × 10^{-4} Pa and then filled with Ar gas to a total working pressure of 0.35 Pa. The magnetron power densities were kept at 10.2 W·cm^{-2} and 6.7 W·cm^{-2} for Cr and ZrB_2, respectively. In the case of the Ag target, the magnetron power density varied in the range of 0–0.3 W·cm^{-2}.

The morphology and thickness characterization of cross-sections of the $Zr_{1-x}Ag_xB_2$ samples was performed by scanning electron microscopy (SEM, Thermofisher Scientific Apreo 2, Waltham, MA, USA). The chemical composition of the films was measured by wave dispersive X-ray spectroscopy (SEM, Tescan Lyra—WDS, INCA Oxford Instruments, Abingdon, UK) calibrated with a mirror-polished ZrB_2 standard. Phase analysis was carried out via X-ray diffraction (XRD) in the Bragg–Brentano (BB) and grazing incidence (GI) geometry using a PANalytical X'pert diffractometer (Malvern, UK) equipped with CuKα (λ = 0.15418 nm). Nanoindentation hardness H and Young's modulus E were measured using a nanoindenter (Anton Paar NHT^2, Graz, Austria) equipped with a Berkovich diamond tip. The applied load was varied from 2 to 10 mN to not exceed the indentation depth of 10% of the film thickness (~1.2–1.5 µm), thus avoiding substrate influence. H and E were determined via the Oliver and Phaar method [33]. The presented results are averages from a total of 16 measurements (4 × 4 patterns). Standard deviations for the measurements are presented in the form of error bars. In order to analyze enhanced ductility, a nanoindenter (Anton Paar NHT^2) equipped with a diamond cube-corner tip was used. A total of 9 indentations were performed at each sample to minimize statistical error from any inhomogeneity for different loads from 20 mN to 100 mN to obtain similar indents for samples with different hardness.

The coefficient of friction (COF) was measured by a tribometer (Bruker UMT/2, Billerica, MA, USA) by the ball-on-disc method, and wear tracks were evaluated by SEM. The measurements were carried out against steel (100Cr6), Si_3N_4, and WC/Co (6 wt.% of cobalt) balls in ambient conditions with a relative humidity of 45%–50% and a load of 5 N and a total time of measurement 3600 s. For steel balls, the time of measurement was shortened to half due to their low resistance to wear. For wear-track analysis, the measurement time was set to 600 s due to the total wear of samples with a high amount of silver at 3600 s measurement.

3. Results and Discussion

3.1. Calculation Results

In this study, ab initio DFT calculations were implemented to investigate the stability and elastic properties of hexagonal α-$Zr_{1-x}Ag_xB_2$. With the increase in x (Ag content), the formation energy E_f (Figure 1a) gradually increases, indicating that the system is converting into a less structurally stable one. The $Zr_{0.375}Ag_{0.625}B_2$ already has a positive value of E_f, which suggests strong structural instability. The values of mixing enthalpies ΔH_{mix} (Figure 1b) calculated with respect to ZrB_2 and AgB_2 are positive in the whole concentration range. Moreover, the values only slightly differ with increasing temperature, pointing to strong insolubility even in the state at 0 K with only a minor contribution from increasing temperature. Similar behavior/tendencies were theoretically predicted and experimentally observed on the similar $TiAlB_2$ and $ZrAlB_2$ systems [9,15]. In the $ZrAlB_2$ system, a more moderate trend in values of E_f and ΔH_{mix} led to the formation of a dual structure. As-dep samples with 8 at.% of alloying metal contained a decomposed solid solution. Therefore, a similar structure is expected in $Zr_{1-x}Ag_xB_{2+\Delta}$ even at such low Ag content. Systems with an amount of x > 0.625 do not meet the necessary conditions [34] for mechanical stability; therefore, they will not be further considered. Structural analysis reveals an almost linear increase of the c lattice parameter, as was expected. Due to the presence of strong covalent B-B bonds in (000z) planes, the c parameter has a tendency to expand more. The lattice parameter a is slightly decreased upon silver alloying.

From the view of theoretically obtained elastic properties, all of the investigated polycrystalline moduli—Young's moduli (E), shear moduli (G), and bulk moduli (B)—linearly decrease with an increasing amount of Ag from E^{ZrB2} = 494 GPa to $E^{Zr0.375Ag0.625B2}$ = 210 GPa (decrease of 58%), G^{ZrB2} = 216 GPa to $G^{Zr0.375Ag0.625B2}$ = 81 GPa (decrease of 63%), and B^{ZrB2} = 230 GPa to $B^{Zr0.375Ag0.625B2}$ = 183 GPa (decrease of 21%). Moreover, with increasing Ag amount, hardness also drastically decreases from H^{ZrB2} = 40 GPa to $H^{Zr0.375Ag0.625B2}$ = 7 GPa (decrease of 83%). Ductile/brittle behavior is non-directly investigated from the values of

Pugh's ratio G/B, Poisson's ratio, and Cauchy's pressures of C_{13}-C_{44} (0001) and C_{12}-C_{66} (10-10). Therefore, from Table 1, a tendency toward ductile behavior with increasing Ag amount can be seen. Specifically, G/B increases from $G/B^{ZrB2} = 0.94$ to $G/B^{Zr0.375Ag0.625B2} = 0.44$ (crossing the critical empirical value of 0.57 between brittle and ductile materials). As Poisson's ratio increases from $\nu^{ZrB2} = 0.14$ to $\nu^{Zr0.375Ag0.625B2} = 0.3$ (crossing the critical empirical value of 0.26 between brittle and ductile materials), Cauchy's pressures increase from C_{12}-$C_{66}{}^{ZrB2} = -113$ GPa to C_{12}-$C_{66}{}^{Zr0.375Ag0.625B2} = 75$ GPa (10-10) and from C_{13}-$C_{44}{}^{ZrB2} = -113$ GPa -184 to C_{13}-$C_{44}{}^{Zr0.375Ag0.625B2} = -60$ GPa (positive values indicate ductile behavior). Tribological behavior was investigated via analysis of machinability index parameter $\mu_m = B/C_{44}$. As can be clearly seen from Table 1, μ_m increases from $\mu_m{}^{ZrB2} = 0.98$ to $\mu_m{}^{Zr0.375Ag0.625B2} = 6.34$, indicating very promising development of tribological properties upon Ag alloying, where from the experimental point of view, significant reduction of coefficient of friction can be expected.

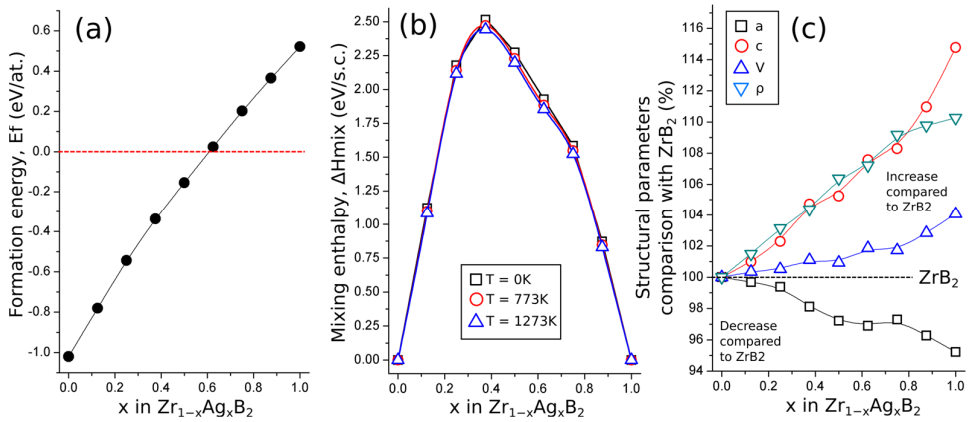

Figure 1. (**a**) Energy of formation (E_f) and (**b**) mixing enthalpy (ΔH_{mix}) of α-$Zr_{1-x}Ag_xB_2$ solid solution as a function of Ag content (x), where the red circle and blue triangle illustrate the impact of the temperature of 773 K and 1273 K on ΔH_{mix}, respectively. (**c**) Relative values of the hexagonal lattice parameters (a, c) with volume (V) and density (ρ) as a function of Ag content (x) compared with reference ZrB_2.

Table 1. Computed elastic properties of ZrB_2 and $Zr_{1-x}Ag_xB_2$ solid solutions with respect to Ag content (x). Specifically, E, G, B, ν, and H denote the elastic modulus, shear modulus, bulk modulus, Poisson's ratio, and Vickers hardness, respectively, while B/C_{44} is the machinability index, C_{12}-C_{66} and C_{13}-C_{44} are directional Cauchy pressures in the hexagonal (0001) and (10-10) directions and G/B denotes Pugh's ratio.

System	E (GPa)	G (GPa)	B (GPa)	ν	H (GPa)	μ_m	C_{12}-C_{66} (GPa)	C_{13}-C_{44} (GPa)	G/B
ZrB_2	494	216	230	0.14	40	0.98	−184	−113	0.94
$Zr_{0.875}Ag_{0.125}B_2$	456	196	226	0.16	34	1.19	−156	−78	0.87
$Zr_{0.75}Ag_{0.25}B_2$	387	162	214	0.20	25	1.59	−129	−12	0.76
$Zr_{0.625}Ag_{0.375}B_2$	321	130	203	0.24	17	2.18	−114	29	0.64
$Zr_{0.5}Ag_{0.5}B_2$	283	112	197	0.26	13	3.11	−90	43	0.57
$Zr_{0.375}Ag_{0.625}B_2$	210	81	183	0.30	7	6.35	−60	75	0.44
$Zr_{0.25}Ag_{0.75}B_2$	179	68	176	0.32	5	4.39	−33	46	0.39
$Zr_{0.125}Ag_{0.875}B_2$	86	33	159	0.32	−0.6	−1304	10	78	0.21
AgB_2	−9	−3	147	0.58	-	−33	297	72	−0.02

3.2. Experimental Results

3.2.1. Chemical Composition Analysis

The ab-initio results (presented in Section 3.1) indicate the possible formation of metastable $ZrAgB_2$ solid solutions at Ag concentrations below 21 at.%. In addition, increasing the silver content in $ZrAgB_2$ continuously decreases the hardness, which practically means that only films with an Ag content of less than 15 at.% maintaining relatively high hardness values are usable in a demanding abrasive environment. On the contrary, higher

Ag concentrations are promising from the point of view of tribological properties, and therefore our experimental investigation also includes these compositions.

Quantitative elemental WDS analysis of the reference $ZrB_{2+\Delta}$ film revealed a slightly overstoichiometric B/Zr ratio of 2.3. In the following steps, we prepared $Zr_{1-x}Ag_xB_{2+\Delta}$ films by co-deposition from ZrB_2 and Ag targets. Due to the very high deposition rate of silver, each subtle increase in the power density on the Ag target led to a significant increase in the Ag content in the $Zr_{1-x}Ag_xB_{2+\Delta}$ films. At the same time, the boron content also decreased, which can be seen in the gradual reduction of the B/(Zr + Ag) ratio from 2.07 to 1.61. However, a relatively high jump of B/(Zr + Ag) to a value of 0.89 can be seen in the sample prepared at the highest power density of 2.4 W/cm^2. This fact can be attributed to the relatively high voltage at the Ag target (470 V). Then, the reflected Ar neutrals can cause resputtering of the growing films [8]. Because the sum of elemental composition is 100 at.%, with increasing Ag content, Zr and B content is reduced relative to Ag. The proportion of impurities (C, O) incorporated in the films is less than 3 ± 1 at.% which is a relatively high but common value for ZrB_2 thin films due to the high affinities of Zr and B to oxygen [35–37]. Because our base pressure is below 5×10^{-4} Pa, we assume that contaminants originate from the target material. With increasing power density on the Ag target, deposition time was optimized to obtain a similar thickness of all samples of ~1.2–1.5 µm. The authors of the manuscript are aware of the sensitivity of WDS analysis to light elements that bond in various coordination and WDS accuracy compared with different analytical methods [38]. In the case of WDS analysis, the B/metals ratio is affected by systematic error. However, every measurement is equally laden with error, thus, we assume that trends are correct and relative values within the deposition series are comparable. The uncertainty shown in Table 2 refers to the typical standard deviation of five measurements across different sites of the sample, not the uncertainty due to the precision and systematic error of WDS analysis.

Table 2. WDS quantitative elemental analysis of $ZrB_{2+\Delta}$ and $Zr_{1-x}Ag_xB_{2+\Delta}$ films with deposition current (I), voltage (U), and power density on the Ag target.

I (A)	U (V)	P (W/cm^2)	Zr (at.%)	Ag (at.%)	B (at.%)	B/(Zr + Ag)
0	0	0	29.6 ± 1	0	68.4 ± 1	2.31
0.05	338	0.22	29.5 ± 1	2.2 ± 1	65.8 ± 1	2.07
0.07	350	0.31	27.4 ± 1	8.0 ± 1	61.4 ± 1	1.74
0.1	374	0.48	23.9 ± 1	12.6 ± 1	61.0 ± 1	1.67
0.2	415	1.06	17.5 ± 1	19.8 ± 1	59.9 ± 1	1.61
0.4	470	2.39	13.9 ± 1	39.0 ± 1	47.2 ± 1	0.89

3.2.2. Structure and Morphology Analysis

Cross-sectional SEM images of the $ZrB_{2.31}$ film sputtered from a single ZrB_2 target show featureless fracture morphology. In our case, low ion energy (due to floating potential) did not result in clear columnar morphology, typical for crystalline ZrB_2 [9,26,39]. SEM fracture images of co-sputtered $Zr_{1-x}Ag_xB_{2+\Delta}$ containing 2 and 8 at.% Ag indicate the presence of columnar morphology (Figure 2). As can be seen, columnar growth is suppressed within the samples with 20 and 39 at.% of Ag. The EDS map of $Zr_{0.65}Ag_{0.35}B_{1.67}$ film reveals chemically separated Zr-rich and Ag-rich regions, suggesting structure segregation and the formation of a dual structure. Unfortunately, such an investigation was not carried out in samples with 2 and 8 at.% due to the insufficient signal from the low number of Ag atoms.

Figure 3a shows a series of XRD θ/2θ diffraction patterns of as-deposited $ZrB_{2+\Delta}$ and $Zr_{1-x}Ag_xB_{2+\Delta}$ films with different silver contents. The X-ray pattern of the reference as-dep $ZrB_{2.31}$ film shows a broad reflection centered near the table value of 2θ~42° for the (101) reflection of the hexagonal (P6/mmm) α-ZrB_2 phase. This broadening indicates a very fine nanocrystalline nature of the structure. The dominant cubic (Im-3m) Cr reflection was also recognized at 2θ~44.1°, belonging to the buffer layer. In the case of Ag-alloyed films, XRD patterns also show a peak at 2θ = 25°, belonging to the reflection (001) from

the α-ZrB_2 phase. With increasing silver content in the films, the intensity of the dominant cubic reflection (Fm-3m) belonging to silver at 2θ~44.3° increases. However, this reflection is very close to the cubic (110) Cr reflection, so in the case of lower silver contents, it is not possible to evaluate with certainty the solubility of Ag in the ZrB_2 grains or its segregation from BB. In the case of $Zr_{0.65}Ag_{0.35}B_{1.67}$ (Ag~12.6 at.%), the reflection located at 2θ~38.1° belonging to silver (111) begins to dominate. The coexistence of ZrB_2 and Ag phases is in good agreement with SEM fractures according to EDS analysis (Figure 2). To suppress dominant Cr (110) buffer layer reflection, the GIXRD method was used. As can be seen from Figure 3b, the reflection located at 2θ~44.1° is still present after the suppression of the signal from the Cr buffer layer in the sample with 2 at.% of Ag ($Zr_{0.93}Ag_{0.07}B_{2.07}$), which suggests phase separation even at such low Ag content. The presence of Ag (111) reflection is also recognizable in the sample with 8 at.% of Ag. However, complete suppression of the signal from the buffer layer is not possible. Due to the overlay of Cr–Ag reflections, a wider range GIXRD of $Zr_{0.93}Ag_{0.07}B_{2.07}$ is provided in Figure 3c, where the increased signal in the position of Ag (111) reflection is noticeable.

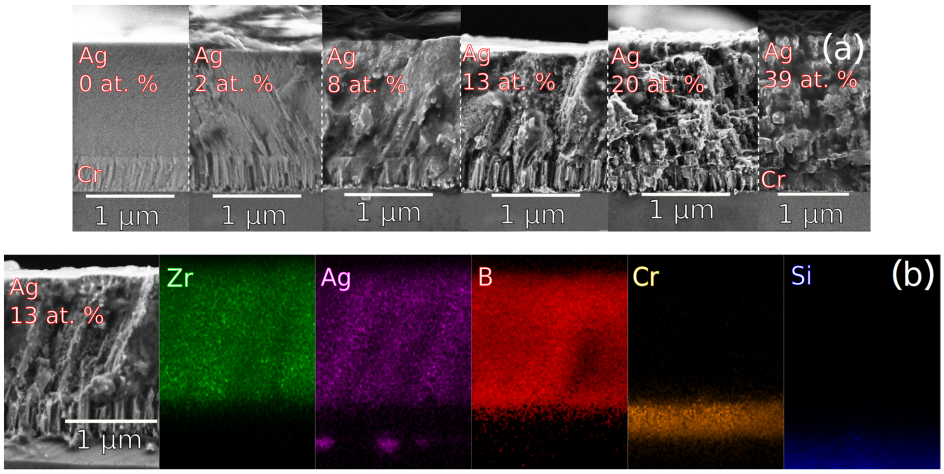

Figure 2. (**a**) Cross-sectional micrographs of $ZrB_{2+\Delta}$ and $Zr_{1-x}Ag_xB_{2+\Delta}$ films and (**b**) $Zr_{0.65}Ag_{0.35}B_{1.67}$ (13 at.% Ag) cross-sectional micrograph with corresponding EDS map of elemental distribution.

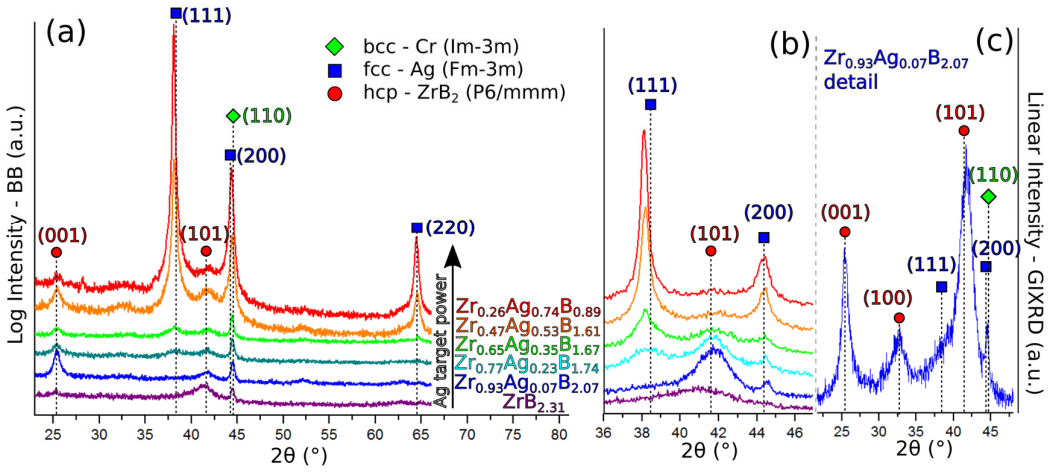

Figure 3. (**a**) Bragg–Brentano XRD patterns of reference $ZrB_{2+\Delta}$ and $Zr_{1-x}Ag_xB_{2+\Delta}$ films, (**b**) grazing incidence XRD detail on selected reflections indicating presence of segregated Ag phase even at 2 at.% of Ag content, and (**c**) grazing incidence XRD detail $Zr_{0.93}Ag_{0.07}B_{2.07}$ pointing out at the presence of (111) Ag reflection.

3.2.3. Mechanical and Tribological Properties

According to the results presented in Figure 4, the hardness values of alloyed $Zr_{1-x}Ag_xB_{2+\Delta}$ films are significantly decreased compared with those of very hard $ZrB_{2.31}$ due to the reduction of cohesive strength at the interfaces between grains. This trend is in good agreement with DFT predictions. We can see a decrease in hardness from a value of $H^{ZrB2.31} = 30 \pm 2$ GPa to $H^{Zr0.26Ag0.74B0.89} = 4.2 \pm 0.9$ GPa (decrease of 86%). The lower hardness of $ZrB_{2.31}$, compared with that of other studies and DFT calculations [9,26], can be explained by the absence of crystalline structure (mainly the presence of (001) texture, typically responsible for high hardness) [8,10] and the overstoichiometry of our samples. The lowered values of Young's modulus non-directly indicate improvement in ductility, again correlating to ab-initio calculations, where the experimental value of Young's modulus decreased from $E^{ZrB2.31} = 375 \pm 13$ GPa to $E^{Zr0.26Ag0.74B0.89} = 154 \pm 18$ GPa (59% decrease).

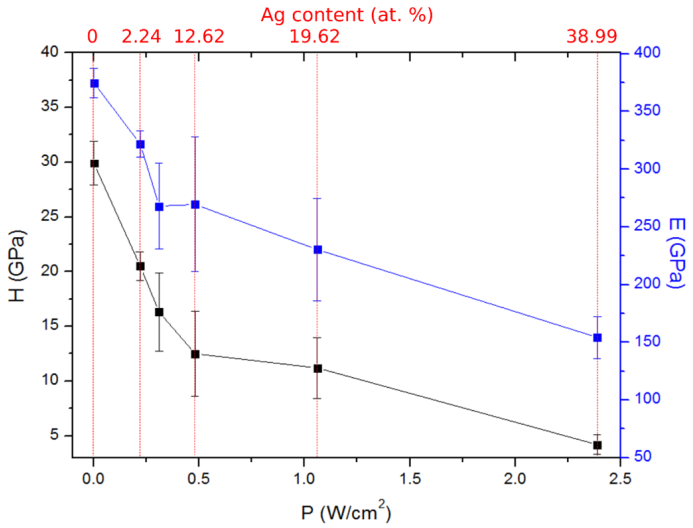

Figure 4. Experimental hardness (H) and Young's moduli (E) of the reference $ZrB_{2+\Delta}$ and $Zr_{1-x}Ag_xB_{2+\Delta}$ films plotted as a function of the power density on Ag target and Ag content.

Cube-corner indents of the reference $ZrB_{2+\Delta}$ and $Zr_{1-x}Ag_xB_{2+\Delta}$ films are shown in Figure 5. In pure $ZrB_{2+\Delta}$, the presence of clear radial cracks can be observed. With increasing Ag content, a reduction in crack length, circular corrugation, and accumulation of material that can be attributed to increased toughness can be seen.

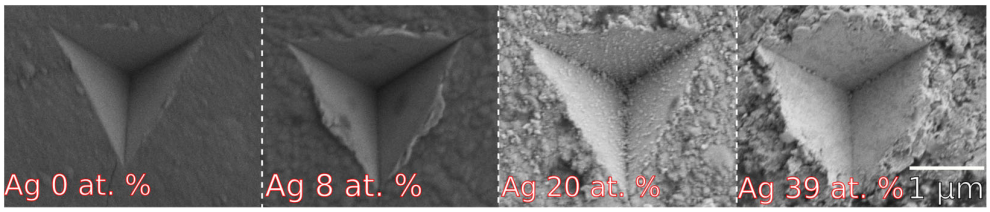

Figure 5. Top view on the cube-corner nanoindentations of the reference $ZrB_{2+\Delta}$ and $Zr_{1-x}Ag_xB_{2+\Delta}$ films.

Results of ball-on-disc tribotests against different types of ball-sliding or counter material can be seen in Figure 6. Due to similar behavior, regardless of the choice of substrate material, tribotest results on the S600 substrate are not shown to preserve the clarity of the figures. As can be clearly seen, Ag-alloying positively impacts COF decrease compared with all materials. High saturated values of COF ~0.9 for pure ZrB_2 were measured against steel and Si_3N_4. However, a lower COF ~0.8 was observed against WC/Co. As we assumed, the lower COF of ZrB_2-WC/Co tribocontact can be explained by higher flash temperatures during measurement. The higher hardness of the WC/Co counterpart compared with ceramic Si_3N_4 may lead to the formation of the lubricating

B_2O_3 which can occur even at room temperature [20]. During the tribo test, heat generation occurs. The generated heat is sufficient to start the oxidation of the ZrB_2, when ZrB_2 is reacting with $5/2O_2$ into ZrO_2 and B_2O_3. The oxygen required for the reaction is available from the surrounding air [20]. This assumption is supported by the WDS analysis in Figure 6d which indicates a higher concentration of oxygen within the wear track worn by WC/Co compared with other counterparts used. The uncertainty shown in Figure 6d refers to the standard deviation of five measurements from different sites on the wear track. Alloying with 8 at.% of Ag leads to a decrease in COF in the case of Si_3N_4 to a value of 0.65 and in the case of WC/Co to a value of 0.45. The sample with 8 at.% of Ag against steel shows still relatively high COF with a value of 0.75. Such a value can be explained by the lower temperatures during measurement against the steel counterpart with the lower hardness value compared with those of Si_3N_4 and WC/Co. The lowering of COF, in general, can be attributed to the lubricating properties of silver itself. Still, due to the small amount of silver, no visible change was seen in SEM wear track analysis.

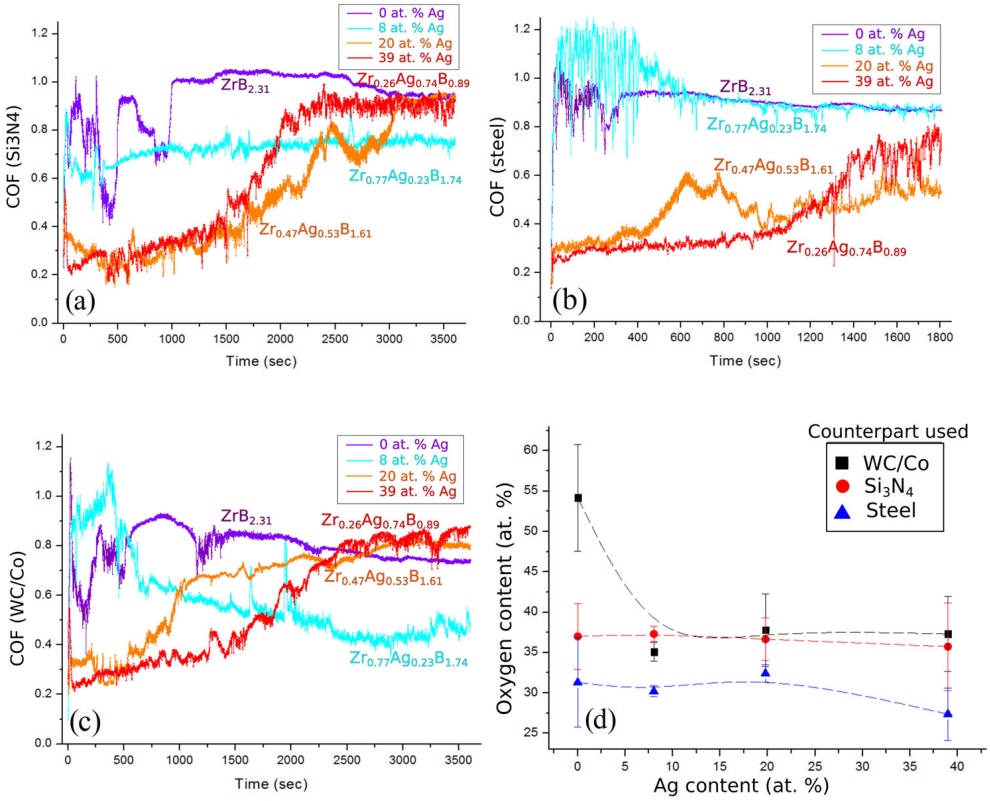

Figure 6. Results of dry sliding ball-on-disc tribological test for the reference $ZrB_{2+\Delta}$ and $Zr_{1-x}Ag_xB_{2+\Delta}$ films on K100 substrate against different ball materials including (**a**) Si_3N_4, (**b**) steel, (**c**) WC/Co and (**d**) analysis of oxygen content in the wear track areas, where Ag content refers to content in films according to Table 2.

Further increase of Ag amount to 20 at.% and 39 at.% resulted in a significant decrease of COF against all counterpart materials to the lowest value of COF ~0.25. As we assumed, lubricating properties and better thermal conductivity of Ag resulted in lower flash temperatures during the tribotest, insufficient for B_2O_3 formation, which is supported by lower oxygen concentration in the wear tracks (Figure 6d). However, phase analysis of oxides by the X-ray diffraction methods was not feasible. Due to the low volume of wear track compared with irradiated volume, diffraction peaks belonging to B- and Zr- oxides were absent in the diffraction pattern. The hump within the values of COF for the sample with 20 at.% can be explained through the accumulation of material during measurement. The change from tribo-chemical reaction to abrasive wear mechanism due to increased Ag

concentration can be seen in Figure 7, where clear abrasive grooves are shown in the details of $Zr_{0.26}Ag_{0.74}B_{0.84}$ wear tracks. Due to the low hardness values of $Zr_{0.47}Ag_{0.53}B_{1.61}$ and $Zr_{0.26}Ag_{0.74}B_{0.89}$, an increase in COF can be seen in all cases caused by total wear out of the coatings. Therefore, shorter measurements of 600 s had to be conducted for correct wear track SEM analysis.

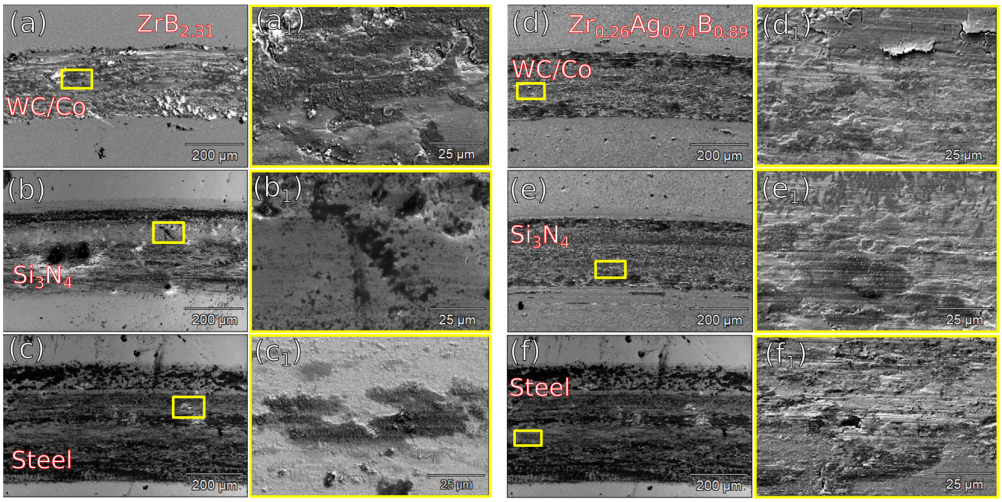

Figure 7. Wear tracks of $ZrB_{2.31}$ sample from the view of SEM worn against different counterpart materials: (**a**) WC/Co, (**b**) Si_3N_4, (**c**) Steel. Details of these wear tracks ((**a$_1$**) WC/Co, (**b$_1$**) Si_3N_4, and (**c$_1$**) steel) and wear tracks of $Zr_{0.26}Ag_{0.74}B_{0.89}$ from the view of SEM against different counterpart material ((**d**) WC/Co, (**e**) Si_3N_4, and (**f**) steel), with corresponding wear track details ((**d$_1$**) WC/Co, (**e$_1$**) Si_3N_4, and (**f$_1$**) steel).

4. Conclusions

In the present study, the DFT calculations were employed to investigate the effect of silver alloying on the structural and chemical stability and mechanical properties of the hexagonal $Zr_{1-x}Ag_xB_2$ system. The calculations point out the strong insolubility of silver in $Zr_{1-x}Ag_xB_2$ over the whole concentration range. Increasing silver content leads to a decrease in hardness, Young's, bulk, and shear moduli. The improvement of ductility was also indirectly supported by an increase in Cauchy pressures and Poisson's ratio and a decrease in Pugh's ratio. Calculations also suggest improvements in tribological properties where the machinability index μ_m was increased upon silver alloying.

Motivated by the computational results, we experimentally prepared $Zr_{1-x}Ag_xB_{2\pm\Delta}$ with different silver contents using magnetron co-sputtering. For Ag concentrations above 12 at.%, analysis suggests the formation of a dual structure with the columnar character of segregated hexagonal α-ZrB_2 and cubic Ag structure. Further structural analysis confirmed the formation of a dual structure in the sample with a silver content of 2 at.%.

As was predicted by the ab-initio calculations, Ag alloying led to a decrease in hardness values from $H^{ZrB2.31}$ = 30 GPa to $H^{Zr0.26Ag0.74B0.89}$ = 4.2 GPa, followed by a decrease of $E^{ZrB2.31}$ = 375 GPa to $E^{Zr0.26Ag0.74B0.89}$ = 154 GPa. Improvement in toughness and ductile behavior was experimentally confirmed by cube-corner indentations, where the crack formation was suppressed with increasing Ag content.

Further motivated by the calculations, tribological properties via the ball-on-disc method were investigated. Based on the counterpart material used, the coefficient of friction decreased with an increasing amount of silver, with the most significant improvement being a reduction from 0.95 for ZrB_2 to 0.25 for the sample with 39 at.% Ag. Further analysis indicates a change in wear from tribo-oxidative to abrasive, indicating positive lubricant properties upon silver alloying.

Author Contributions: Conceptualization, T.F. and M.T.; validation, T.F. and M.T.; methodology T.F. and M.M.; investigation, T.F., M.T., V.Š., T.R., V.I., M.V., M.H. and L.S.; resources, M.M.; data curation, T.F.; writing—original draft preparation, T.F. and M.M.; writing—review and editing, T.F., M.T., T.R., V.I., M.V., M.H. and M.M.; visualization, T.F. and M.M.; supervision, M.T. and M.M.; project administration, M.M. All authors have read and agreed to the published version of the manuscript.

Funding: This work was supported by an Operational Program Integrated Infrastructure (Project No. ITMS 313011AUH4).

Data Availability Statement: The data presented in this study are available from the corresponding author upon reasonable request.

Conflicts of Interest: The authors declare no conflict of interest.

References

1. Magnuson, M.; Hultman, L.; Högberg, H. Review of Transition-Metal Diboride Thin Films. *Vacuum* **2022**, *196*, 110567. [CrossRef]
2. Fahrenholtz, W.G.; Hilmas, G.E.; Talmy, I.G.; Zaykoski, J.A. Refractory Diborides of Zirconium and Hafnium. *J. Am. Ceram. Soc.* **2007**, *90*, 1347–1364. [CrossRef]
3. Kurbatkina, V.V.; Patsera, E.I.; Levashov, E.A.; Timofeev, A.N. Self-Propagating High-Temperature Synthesis of Refractory Boride Ceramics (Zr,Ta)B2 with Superior Properties. *J. Eur. Ceram. Soc.* **2018**, *38*, 1118–1127. [CrossRef]
4. Gild, J.; Zhang, Y.; Harrington, T.; Jiang, S.; Hu, T.; Quinn, M.C.; Mellor, W.M.; Zhou, N.; Vecchio, K.; Luo, J. High-Entropy Metal Diborides: A New Class of High-Entropy Materials and a New Type of Ultrahigh Temperature Ceramics. *Sci. Rep.* **2016**, *6*, 37946. [CrossRef]
5. Mayrhofer, P.H.; Mitterer, C.; Clemens, H. Self-Organized Nanostructures in Hard Ceramic Coatings. *Adv. Eng. Mater.* **2005**, *7*, 1071–1082. [CrossRef]
6. Mikula, M.; Grančič, B.; Roch, T.; Plecenik, T.; Vávra, I.; Dobročka, E.; Šatka, A.; Buršíková, V.; Držík, M.; Zahoran, M.; et al. The Influence of Low-Energy Ion Bombardment on the Microstructure Development and Mechanical Properties of TiBx Coatings. *Vacuum* **2011**, *85*, 866–870. [CrossRef]
7. Neidhardt, J.; Mráz, S.; Schneider, J.M.; Strub, E.; Bohne, W.; Liedke, B.; Möller, W.; Mitterer, C. Experiment and Simulation of the Compositional Evolution of Ti–B Thin Films Deposited by Sputtering of a Compound Target. *J. Appl. Phys.* **2008**, *104*, 063304. [CrossRef]
8. Šroba, V.; Fiantok, T.; Truchlý, M.; Roch, T.; Zahoran, M.; Grančič, B.; Švec, P.; Nagy, Š.; Izai, V.; Kúš, P.; et al. Structure Evolution and Mechanical Properties of Hard Tantalum Diboride Films. *J. Vac. Sci. Technol. A* **2020**, *38*, 033408. [CrossRef]
9. Fiantok, T.; Šroba, V.; Koutná, N.; Izai, V.; Roch, T.; Truchlý, M.; Vidiš, M.; Satrapinskyy, L.; Nagy, Š.; Grančič, B.; et al. Structure Evolution and Mechanical Properties of Co-Sputtered Zr-Al-B_2 Thin Films. *J. Vac. Sci. Technol. A* **2022**, *40*, 033414. [CrossRef]
10. Fuger, C.; Hahn, R.; Zauner, L.; Wojcik, T.; Weiss, M.; Limbeck, A.; Hunold, O.; Polcik, P.; Riedl, H. Anisotropic Super-Hardness of Hexagonal $WB_{2\pm z}$ Thin Films. *Mater. Res. Lett.* **2022**, *10*, 70–77. [CrossRef]
11. Nedfors, N.; Tengstrand, O.; Lu, J.; Eklund, P.; Persson, P.O.Å.; Hultman, L.; Jansson, U. Superhard NbB2− Thin Films Deposited by Dc Magnetron Sputtering. *Surf. Coat. Technol.* **2014**, *257*, 295–300. [CrossRef]
12. Yalamanchili, K.; Schramm, I.C.; Jiménez-Piqué, E.; Rogström, L.; Mücklich, F.; Odén, M.; Ghafoor, N. Tuning Hardness and Fracture Resistance of ZrN/Zr0.63Al0.37N Nanoscale Multilayers by Stress-Induced Transformation Toughening. *Acta Mater.* **2015**, *89*, 22–31. [CrossRef]
13. Hahn, R.; Bartosik, M.; Soler, R.; Kirchlechner, C.; Dehm, G.; Mayrhofer, P.H. Superlattice Effect for Enhanced Fracture Toughness of Hard Coatings. *Scr. Mater.* **2016**, *124*, 67–70. [CrossRef]
14. Buchinger, J.; Koutná, N.; Chen, Z.; Zhang, Z.; Mayrhofer, P.H.; Holec, D.; Bartosik, M. Toughness Enhancement in TiN/WN Superlattice Thin Films. *Acta Mater.* **2019**, *172*, 18–29. [CrossRef]
15. Nedfors, N.; Mráz, S.; Palisaitis, J.; Persson, P.O.Å.; Lind, H.; Kolozsvari, S.; Schneider, J.M.; Rosen, J. Influence of the Al Concentration in Ti-Al-B Coatings on Microstructure and Mechanical Properties Using Combinatorial Sputtering from a Segmented TiB2/AlB2 Target. *Surf. Coat. Technol.* **2019**, *364*, 89–98. [CrossRef]
16. Bakhit, B.; Engberg, D.L.J.; Lu, J.; Rosen, J.; Högberg, H.; Hultman, L.; Petrov, I.; Greene, J.E.; Greczynski, G. Strategy for Simultaneously Increasing Both Hardness and Toughness in ZrB_2-Rich $Zr_{1-x}Ta_xB_y$ Thin Films. *J. Vac. Sci. Technol. A* **2019**, *37*, 031506. [CrossRef]
17. Umeda, K.; Enomoto, Y.; Mitsui, A.; Mannami, K. Friction and Wear of Boride Ceramics in Air and Water. *Wear* **1993**, *169*, 63–68. [CrossRef]
18. Bhatt, B.; Murthy, T.S.R.C.; Limaye, P.K.; Nagaraj, A.; Singh, K.; Sonber, J.K.; Sairam, K.; Sashanka, A.; Rao, G.V.S.N.; Rao, T.S. Tribological Studies of Monolithic Chromium Diboride against Cemented Tungsten Carbide (WC–Co) under Dry Condition. *Ceram. Int.* **2016**, *42*, 15536–15546. [CrossRef]
19. Lofaj, F.; Moskalewicz, T.; Cempura, G.; Mikula, M.; Dusza, J.; Czyrska-Filemonowicz, A. Nanohardness and Tribological Properties of Nc-TiB2 Coatings. *J. Eur. Ceram. Soc.* **2013**, *33*, 2347–2353. [CrossRef]

20. Sonber, J.K.; Raju, K.; Murthy, T.S.R.C.; Sairam, K.; Nagaraj, A.; Majumdar, S.; Kain, V. Friction and Wear Properties of Zirconium Diboride in Sliding against WC Ball. *Int. J. Refract. Met. Hard Mater.* **2018**, *76*, 41–48. [CrossRef]
21. Medved', D.; Balko, J.; Sedlák, R.; Kovalčíková, A.; Shepa, I.; Naughton-Duszová, A.; Bączek, E.; Podsiadło, M.; Dusza, J. Wear Resistance of ZrB2 Based Ceramic Composites. *Int. J. Refract. Met. Hard Mater.* **2019**, *81*, 214–224. [CrossRef]
22. Mallik, M.; Mitra, P.; Srivastava, N.; Narain, A.; Dastidar, S.G.; Singh, A.; Paul, T.R. Abrasive Wear Performance of Zirconium Diboride Based Ceramic Composite. *Int. J. Refract. Met. Hard Mater.* **2019**, *79*, 224–232. [CrossRef]
23. Aouadi, S.M.; Bohnhoff, A.; Sodergren, M.; Mihut, D.; Rohde, S.L.; Xu, J.; Mishra, S.R. Tribological Investigation of Zirconium Nitride/Silver Nanocomposite Structures. *Surf. Coat. Technol.* **2006**, *201*, 418–422. [CrossRef]
24. Fenker, M.; Balzer, M.; Kellner, S.; Polcar, T.; Richter, A.; Schmidl, F.; Vitu, T. Formation of Solid Lubricants during High Temperature Tribology of Silver-Doped Molybdenum Nitride Coatings Deposited by DcMS and HIPIMS. *Coatings* **2021**, *11*, 1415. [CrossRef]
25. Sliney, H.E. The Use of Silver in Self-Lubricating Coatings for Extreme Temperatures. *ASLE Trans.* **1986**, *29*, 370–376. [CrossRef]
26. Tengdelius, L.; Broitman, E.; Lu, J.; Eriksson, F.; Birch, J.; Nyberg, T.; Hultman, L.; Högberg, H. Hard and Elastic Epitaxial ZrB2 Thin Films on Al2O3(0001) Substrates Deposited by Magnetron Sputtering from a ZrB2 Compound Target. *Acta Mater.* **2016**, *111*, 166–172. [CrossRef]
27. Blöchl, P.E. Projector Augmented-Wave Method. *Phys. Rev. B* **1994**, *50*, 17953–17979. [CrossRef]
28. Giannozzi, P.; Baroni, S.; Bonini, N.; Calandra, M.; Car, R.; Cavazzoni, C.; Ceresoli, D.; Chiarotti, G.L.; Cococcioni, M.; Dabo, I.; et al. QUANTUM ESPRESSO: A Modular and Open-Source Software Project for Quantum Simulations of Materials. *J. Phys. Condens. Matter.* **2009**, *21*, 395502. [CrossRef]
29. Giannozzi, P.; Andreussi, O.; Brumme, T.; Bunau, O.; Nardelli, M.B.; Calandra, M.; Car, R.; Cavazzoni, C.; Ceresoli, D.; Cococcioni, M.; et al. Advanced Capabilities for Materials Modelling with Quantum ESPRESSO. *J. Phys. Condens. Matter.* **2017**, *29*, 465901. [CrossRef]
30. Zeng, X.; Peng, R.; Yu, Y.; Hu, Z.; Wen, Y.; Song, L. Pressure Effect on Elastic Constants and Related Properties of Ti3Al Intermetallic Compound: A First-Principles Study. *Materials* **2018**, *11*, 2015. [CrossRef]
31. Chen, X.-Q.; Niu, H.; Li, D.; Li, Y. Modeling Hardness of Polycrystalline Materials and Bulk Metallic Glasses. *Intermetallics* **2011**, *19*, 1275–1281. [CrossRef]
32. Chen, K.; Li, C.; Hu, M.; Hou, X.; Li, C.; Chen, Z. Deformation Modes and Anisotropy of Anti-Perovskite Ti3AN (A = Al, In and Tl) from First-Principle Calculations. *Materials* **2017**, *10*, 362. [CrossRef]
33. Oliver, W.C.; Pharr, G.M. An Improved Technique for Determining Hardness and Elastic Modulus Using Load and Displacement Sensing Indentation Experiments. *J. Mater. Res.* **1992**, *7*, 1564–1583. [CrossRef]
34. Mouhat, F.; Coudert, F.-X. Necessary and Sufficient Elastic Stability Conditions in Various Crystal Systems. *Phys. Rev. B* **2014**, *90*, 224104. [CrossRef]
35. Chakrabarti, U.K.; Barz, H.; Dautremont-Smith, W.C.; Lee, J.W.; Kometani, T.Y. Deposition of Zirconium Boride Thin Films by Direct Current Triode Sputtering. *J. Vac. Sci. Technol. A Vac. Surf. Film.* **1987**, *5*, 196–201. [CrossRef]
36. Guziewicz, M.; Piotrowska, A.; Turos, A.; Mizera, E.; Winiarski, A.; Szade, J. Characteristics of Sputter-Deposited TiN, ZrB2 and W2B Diffusion Barriers for Advanced Metallizations to GaAs. *Solid-State Electron.* **1999**, *43*, 1055–1061. [CrossRef]
37. Shappirio, J.R.; Finnegan, J.J. Synthesis and Properties of Some Refractory Transition Metal Diboride Thin Films. *Thin Solid Films* **1983**, *107*, 81–87. [CrossRef]
38. Bakhit, B.; Primetzhofer, D.; Pitthan, E.; Sortica, M.A.; Ntemou, E.; Rosen, J.; Hultman, L.; Petrov, I.; Greczynski, G. Systematic Compositional Analysis of Sputter-Deposited Boron-Containing Thin Films. *J. Vac. Sci. Technol. A* **2021**, *39*, 063408. [CrossRef]
39. Tengdelius, L.; Samuelsson, M.; Jensen, J.; Lu, J.; Hultman, L.; Forsberg, U.; Janzén, E.; Högberg, H. Direct Current Magnetron Sputtered ZrB2 Thin Films on 4H-SiC(0001) and Si(100). *Thin Solid Films* **2014**, *550*, 285–290. [CrossRef]